

## PHYSICAL PROPERTIES OF THE INNER SHOCKS IN HOT, TILTED BLACK HOLE ACCRETION FLOWS

ALEKSEY GENEROZOV

Department of Astronomy, Columbia University, 550 West 120th Street, New York, NY 10027

OMER BLAES

Department of Physics, University of California, Santa Barbara, Santa Barbara CA 93106

P. CHRIS FRAGILE

Department of Physics and Astronomy, College of Charleston, Charleston, SC 29424

AND

KEN B. HENISEY

Natural Science Division, Pepperdine University, Malibu, CA 90263

## ABSTRACT

Simulations of hot, pressure supported, tilted black hole accretion flows, in which the angular momentum of the flow is misaligned with the black hole spin axis, can exhibit two non-axisymmetric shock structures in the inner regions of the flow. We analyze the strength and significance of these shock structures in simulations with tilt angles of 10 and 15 degrees. By integrating fluid trajectories in the simulations through the shocks, and tracking the variations of fluid quantities along these trajectories, we show that these shocks are strong, with substantial compression ratios, in contrast to earlier claims. However, they are only moderately relativistic. We also show that the two density enhancements resembling flow streams in their shape are in fact merely post-shock compressions, as fluid trajectories cut across, rather than flow along, them. The dissipation associated with the shocks is a substantial fraction ( $\simeq 3 - 12$  percent) of the rest mass energy advected into the hole, and therefore comparable to the dissipation expected from turbulence. The shocks should therefore make order unity changes in the observed properties of black hole accretion flows that are tilted.

*Subject headings:* accretion, accretion disks — black hole physics — MHD — shock waves — turbulence

## 1. INTRODUCTION

Much has been learned concerning the dynamics of black hole accretion flows with magnetorotational (MRI, Balbus & Hawley 1991, 1998) turbulence in recent years through the use of global, general relativistic magnetohydrodynamical (GRMHD) simulations. In cases where the effects of black hole spin are included, most of these simulations have assumed that the angular momentum of the accretion flow is aligned with the black hole spin axis (e.g. De Villiers, Hawley & Krolik 2003; Gammie, McKinney, & Tóth 2003; Krolik, Hawley, & Hirose 2005; Noble, Krolik, & Hawley 2009; Penna et al. 2010). This has been done largely for simplicity, and because turbulent stresses interacting with Lense-Thirring precession have long been believed to align the inner accretion disk with the black hole spin axis (Bardeen & Petterson 1975), at least when the disk is geometrically thin and turbulent stresses are approximately isotropic. How this alignment might really work in geometrically thin disks with MRI turbulence has only begun to be studied very recently (Sorathia, Krolik & Hawley 2013b).

For geometrically thick disks, tilts and warps are generally thought to propagate as waves rather than diffuse in the disk (Papaloizou & Lin 1995). It is then far from clear that an alignment of the inner disk would take place. In fact, GRMHD simulations of misaligned or tilted thick flows extending out to a finite radius undergo global rigid body precession at a frequency de-

termined by the ratio of the radially integrated Lense-Thirring torque to the total angular momentum of the flow (Fragile et al. 2007), but independent of the actual tilt angle. On the other hand, if magnetic fields in the vicinity of the black hole can build up to exert forces that are sufficient to resist accretion, then rapid alignment of the flow by these magnetic fields can take place (McKinney, Tchekhovskoy, & Blandford 2013).

Given that the angular momentum of the fuel source for the accretion disk around a black hole is unlikely to have any causal connection to the black hole spin, it would appear that misaligned or tilted accretion flows could be quite common in nature. This is especially true in the Galactic center source Sgr A\*, which is fueled by winds from surrounding stars (e.g. Cuadra et al. 2006) and orbiting interstellar gas clouds (Gillessen et al. 2012), neither of which can possibly know about the spin axis of the hole. It would be an amazing coincidence if this particular radiatively inefficient flow would happen to be aligned with the black hole spin. Misalignments are also likely to be common for accreting supermassive black holes as new sources of fuel enter the black hole's gravitational sphere of influence. The consequences of this for the evolution of black hole spin in active galactic nuclei has received much recent attention (e.g. King & Pringle 2006; Volonteri, Sikora & Lasota 2007).

In principle, a long-lived fuel source with stable angular momentum, e.g. in an X-ray binary, could torque the black hole spin into alignment given suffi-

cient time, but estimates for how long this would take (e.g. Martin, Tout, & Pringle 2008) depend on the uncertain physics of Lense-Thirring precession combined with MRI turbulence in a geometrically thin disk. Recent hydrodynamic and MHD simulations of geometrically thin, warped disks (Sorathia, Krolik & Hawley 2013a,b) have begun to shed light on this physics, emphasizing the importance of transonic flows that mix angular momenta when warps are nonlinear, and the importance of the fact that magnetorotational turbulent stresses are anisotropic, in contrast to what is generally assumed in alpha-based modeling of warps.

The observational evidence for alignments or misalignments in black hole X-ray binaries is mixed. Measurements of the orientation of the radio jets (Hjellming & Rupen 1995) and the binary orbital angular momentum (Greene, Bailyn & Orosz 2001) of the microquasar GRO J1655-40 suggest a misalignment of greater than 15 degrees. On the other hand, modeling of the observed jet kinematics in XTE J1550-564 by Steiner & McClintock (2012) gives a jet orientation that may be consistent with the binary orbital angular momentum. Given that only the inclination of the binary angular momentum with respect to the line of sight has been measured, not the position angle, they conclude on a statistical basis that the misalignment with the jet axis is less than  $12^\circ$  (90% confidence). As we shall see here, though, even a tilt as small as this can have interesting consequences.

Tilted black hole accretion flows that are hot and geometrically thick exhibit significant dynamical differences compared to their untilted counterparts. Neglecting the small stochastic velocities associated with turbulence, the orbits of fluid elements in tilted flows are eccentric, not circular. At least for modest tilts, the major axes of these eccentric orbits are parallel to the line of nodes between the disk midplane and black hole equatorial plane, and the orientation of these orbits flips by  $180^\circ$  across the disk midplane (Fragile & Blaes 2008). The eccentricity of the orbits increases as one moves inward in radius, implying a convergence of fluid trajectories near their apocenters (Ivanov & Illarionov 1997). As a result, a pair of standing shocks form in the flow on opposite sides of the black hole along the line of nodes, but at high latitude (Fragile & Blaes 2008). The innermost region of the flow near the black hole is also significantly nonaxisymmetric, with two high density arms connecting high latitude regions of the larger thick disk to the black hole (Fragile et al. 2007). Various measures of the average inner truncation radius of the disk are approximately independent of black hole spin, in contrast to the case of untilted accretion disks where these measures of truncation radius decrease with increasing black hole spin (Fragile 2009; Dexter & Fragile 2011). High frequency variability that is enhanced compared to untilted flows is expected because of the interaction of transient clumps and spiral acoustic waves with the nonaxisymmetric standing shocks (Henisey et al. 2009; Henisey, Blaes & Fragile 2012).

A tilted accretion flow necessarily breaks axisymmetry, and so it is not surprising that nonaxisymmetric structures exist. However, the origin and nature of the high density arms in the innermost region is not entirely clear. Fragile et al. (2007) asserted that these arms were

“plunging streams”, based in part on the fact that they appeared to originate from high latitude points that coincided with the generalized innermost stable circular orbit (ISCO) surface for inclined geodesics orbiting at constant coordinate radius. The Mach numbers of the shocks were also claimed to be very modest and described as weak (Fragile & Blaes 2008), though actual measurements of the Mach numbers over the complete shock surfaces were not carried out. The shocks clearly exerted significant torques on the flow and of course generated entropy (Fragile & Blaes 2008; Dexter & Fragile 2011; Henisey, Blaes & Fragile 2012), but a calculation of how much dissipation of accretion power was actually associated with them was not carried out.

It is the purpose of this paper to present a more complete analysis of the dynamics of the high density arms in the innermost regions, and both the dynamics and dissipation of the shocks. We find that the density arms are not in fact coherent streams of material, but rather post-shock compressed regions in the flow (see also Henisey, Blaes & Fragile 2012). Moreover, the shocks themselves are strong, not weak, with upstream Mach numbers as high as  $\simeq 4.7 - 6$ , depending on time, for a  $15^\circ$  tilt. They also dissipate approximately 3 to 12 percent of the available accretion power. The shocks in a tilted accretion flow therefore produce very substantial changes in both the dynamics and thermodynamics compared to an untilted accretion flow, which will likely result in correspondingly significant changes in their observed properties.

This paper is organized as follows. In section 2 we provide a brief overview of the simulations used in our analysis. We measure the fraction of accretion power dissipated in the shocks in section 3, and then explore the dynamical connection between the shocks and the high density arms in the innermost regions in section 4. We present the variation of shock strength with spatial position and with tilt angle in section 5. We summarize our conclusions and briefly discuss the implications in section 6. Throughout this paper, we use a metric with signature  $(- + + +)$ , and except where otherwise specified, we use units where the speed of light and Newton’s gravitational constant are unity:  $c = G = 1$ .

## 2. SIMULATIONS

The GRMHD simulations used in our study are 0910h and 0915h, described and reported on previously by Fragile et al. (2007) and Henisey, Blaes & Fragile (2012), and generated using the *Cosmos++* code (Anninos, Fragile & Salmonson 2005). Both assumed a Kerr spacetime with dimensionless black hole spin  $a/M = 0.9$ , and used Kerr-Schild coordinates (Font, Ibáñez & Papadopoulos 1998), rotated by the desired tilt of the accretion flow (Fragile & Anninos 2005, 2007). The coordinate radius of the horizon for this black hole spin is  $1.44M$ .

The simulations were initialized with a torus with pressure maximum at coordinate radius  $r = 25M$ . A circular geodesic in the equatorial plane of the black hole at this coordinate radius has an orbital period  $t_{\text{orb}} \simeq 791M$ , and this is close to the actual orbital period of the fluid at the initial pressure maximum of the tilted torus. The torus was initialized with poloidal magnetic field lines along isobaric surfaces, together with random perturba-

tions which seeded the growth of the MRI.

The flow was evolved using the internal energy scheme of *Cosmos++* with an artificial viscosity that we review in more detail in section 3 below. Total energy is not conserved in these simulations, as magnetic and kinetic energy losses occur at the grid scale and are not recaptured as in simulations that use a total energy scheme.

The spatial grid used in the simulations consisted of a Kerr-Schild polar coordinate mesh with  $32 \times 32 \times 32$  zones at the base level encompassing all  $4\pi$  steradians. In addition there were two layers of refinement with twice the resolution in each refinement, resulting in a peak resolution equivalent to a simulation with  $128 \times 128 \times 128$  zones. This peak resolution was achieved over the region  $1.41M \leq r \leq 120M$ ,  $0.111\pi \leq \vartheta \leq 0.889\pi$  and  $0 \leq \varphi < 2\pi$  in the tilted Kerr-Schild coordinates.<sup>1</sup> In other words, the peak resolution covered most of the simulation domain except the regions near the polar axes of the tilted Kerr-Schild coordinate system. In addition, grid zones were spaced logarithmically in the radial direction, nonuniformly in the polar direction with a concentration toward the midplane of the original tilted torus, and uniformly in the azimuthal direction. Much more detail on this gridding and other technical aspects of these simulations can be found in Fragile et al. (2007).

We focus here on data in the time range from  $4 t_{\text{orb}}$ , after which MRI turbulence is well-established in the inner regions of the flow near the black hole, to  $10 t_{\text{orb}}$ , the simulation duration. All fluid variable data from the simulations was written out to files 200 times per orbit at the pressure maximum radius  $25M$  of the initial torus. This corresponds to a time of  $\simeq 3.955M$  between data dumps.

### 3. DISSIPATION ASSOCIATED WITH THE SHOCKS

As we noted above, the *Cosmos++* simulations we are analyzing were performed by integrating the internal energy equation, and not a total energy equation. As a result, energy is not fully conserved because of losses of magnetic and kinetic energy at the grid scale. Simulations such as these therefore mimic an accretion flow wherein accretion power is lost by cooling, but in a completely uncontrolled and artificial way. Similar simulations have been done to explore the dynamics of MRI turbulence in untilted accretion flows (e.g. De Villiers, Hawley & Krolik 2003), but using them to explore the dissipation of this turbulence is clearly problematic. One approach has been to adopt proxies such as the square of the electric current density which might track resistive dissipation (Beckwith et al. 2006), or the electromagnetic stress tensor combined with gradients in fluid velocity (Beckwith et al. 2008).

The one aspect of the dissipation that is explicitly treated in our simulations, however, is the dissipation associated with the shocks. The artificial viscosity used in *Cosmos++* is designed to both numerically resolve these shocks and to capture the mechanical energy dissipated into gas internal energy. We can therefore use this artificial viscosity dissipation to measure the likely contribution to the overall dissipation of accretion power by the

large scale shocks formed in tilted accretion flows. We note, however, that because fluid pressure is fundamentally related to dissipative heating in any real accretion flow, energy conserving simulations with or without cooling prescriptions may produce quantitative differences in shock strength and dissipation from the ones we present here. For example, in an energy conserving, radiatively inefficient flow with no significant cooling, the flow will be hotter than that simulated here, and the Mach numbers of the fluid motions may therefore be smaller, possibly resulting in somewhat weaker shocks.

The internal energy equation used in our GRMHD simulations is

$$\partial_t E + \partial_i (EV^i) = -P\partial_t W - (P + Q)\partial_i (WV^i), \quad (1)$$

where  $V^i \equiv u^i/u^t$  is the coordinate three-velocity,  $u^\alpha$  is the fluid four velocity,  $W = (-g)^{1/2}u^t$  is the relativistic boost factor,  $Q$  is the artificial viscosity,  $P$  is the fluid rest frame gas pressure,  $E$  is related to the fluid rest frame internal energy density  $e = P/(\Gamma - 1)$  (excluding rest mass) by  $E = We$ , and  $\Gamma$  is the adiabatic index of the gas (assumed to be  $5/3$  in our simulations). The left hand side of this equation can be rewritten as

$$\partial_t E + \partial_i (EV^i) = (-g)^{1/2} \nabla_\alpha (u^\alpha e) \quad (2)$$

Consequently, when integrated over the duration and volume of the simulation, this term represents the total change in the internal energy of the fluid. The integral of the right hand side of the internal energy equation (1) consists of a pressure term and an artificial viscosity term. The pressure term represents reversible work, while the artificial viscosity term represents irreversible dissipation.

The artificial viscosity used in our simulations is given by (Anninos, Fragile & Salmonson 2005)

$$Q = \begin{cases} I_N \Delta x_{\text{min}} \partial_i V^i (2\Delta x_{\text{min}} \partial_j V^j - 0.3c_s) & \text{if } \partial_k V^k < 0, \\ 0 & \text{otherwise,} \end{cases} \quad (3)$$

where  $\Delta x_{\text{min}}$  is the minimum covariant zone length for the particular grid point under consideration, and  $c_s$  is the relativistic sound speed,

$$c_s = \left[ \frac{\Gamma(\Gamma - 1)P}{\Gamma P + (\Gamma - 1)\rho} \right]^{1/2}, \quad (4)$$

where  $\rho$  is the fluid frame rest mass density. The quantity  $I_N$  is a normalized inertia multiplier,

$$I_N \equiv \frac{1}{g_3^{1/2}} [E + W(\rho + P + \sqrt{3}Q + 2P_B)], \quad (5)$$

where  $P_B$  is the magnetic pressure in the fluid rest frame, and  $g_3$  is the 3-metric determinant.<sup>2</sup> Note that  $I_N$  itself depends on  $Q$ . In the simulation this corresponds to the  $Q$  at the previous time-step. We drop this term in the analysis that follows, as it is difficult to reconstruct from the existing simulation data. We also tried solving equations (3) and (5) simultaneously for  $Q$ , and the results

<sup>2</sup> This formulation of the artificial viscosity is not covariant due to the presence of the coordinate velocity divergence in the definition. We believe that this does not significantly affect the results presented here, but in the future it would be good to test this with a fully covariant formulation of artificial viscosity.

<sup>1</sup> The  $0.075\pi \leq \vartheta \leq 0.925\pi$  limits stated in Fragile et al. (2007) are incorrect, and actually refer to the limits of the concentrated latitude coordinate  $x_2$  in that paper.

of these two approaches were generally consistent within a few percent. However, we occasionally found spurious numerical artifacts (i.e. negative dissipations) when we tried solving the two equations simultaneously.

We integrated the artificial viscosity term  $-Q\partial_i(WV^i)$  in equation (1) over the highest refinement grid portion inside of  $r = 14M$  over all epochs to determine the total dissipation rate associated with the shocks. We then time-averaged this total dissipation rate, and found that it amounts to 6.1 percent of the time-averaged rest mass energy accretion rate  $\dot{M}c^2$  onto the hole for the  $10^\circ$  simulation, and 8.9 percent for the  $15^\circ$  simulation. Figure 1 shows the instantaneous accretion rates, and instantaneous dissipation. It is also useful to measure the instantaneous dissipation rate and scale it with the instantaneous  $\dot{M}c^2$  currently entering the hole. We first smoothed  $\dot{M}c^2$  and the dissipation rate over  $237M \simeq 0.3 t_{\text{orb}}$  time intervals to smooth out high frequency fluctuations. As shown in the bottom panel, the scaled dissipation rate ranges from approximately 3 to 9 percent and 7 to 12 percent of the instantaneous  $\dot{M}c^2$  for the  $10^\circ$  and  $15^\circ$  simulations, respectively. Note that, apart from fluctuations, the accretion rate into the hole generally declines by roughly a factor of two over long time scales, while the dissipation rate shows no such obvious decline. The scaled dissipation rate therefore increases somewhat over time.

That this dissipation is associated with shocks can be seen in Figure 2, which shows the spatial structure of surfaces enclosing regions where ninety percent of the total dissipation occurs in the  $10^\circ$  and  $15^\circ$  simulations. Note that in Figure 2 we restrict the surface to a box that is  $8M$  on each side. The nonaxisymmetric structure due to the presence of the large scale shocks is evident (see also Figures 6 and 7 below). For the purposes of this paper we take these 90 percent surfaces as a working definition of shocks. We note that our 90 percent surfaces are spatially co-located with the entropy generation surfaces discussed in Fragile & Blaes (2008); Henisey, Blaes & Fragile (2012).

The spatial extent of the shocks is actually increasing slowly with time throughout the course of both the  $10^\circ$  and  $15^\circ$  simulation. Because of this, the shocks are able to dissipate a larger fraction of the energy in the flow as time goes on. In the case of the  $10^\circ$  simulation, this more than compensates for the declining accretion rate from 4 to 7 orbits, so that the volume integrated dissipation rate increases over this time period. Later on, the increased spatial volume of the shocked regions appears to just compensate for the declining accretion rate, and this is also true throughout the  $15^\circ$  simulation, so that the dissipation rate is roughly constant.

To address how much of this power escapes the vicinity of the black hole requires an understanding of how that power might be emitted as photons, and how many of those photons will reach an observer at infinity (Dexter & Fragile 2011, 2013). As a crude estimate of this, Figure 1 also shows the time dependence of the scaled volume-integrated dissipation rate in both simulations, but excluding regions inside the coordinate radius of the direct equatorial photon orbit, as it is likely that emission from inside this orbit will not reach infinity. The dissipation rates outside the photon orbit are less than

the previous estimates of the total dissipation rates, but only slightly: 3 to 9 percent and 6 to 10 percent of the instantaneous  $\dot{M}c^2$  for the  $10^\circ$  and  $15^\circ$  simulations, respectively.

These scaled dissipation rates should be compared with the binding energy per unit rest mass of the equatorial ISCO orbit, which is commonly used as an estimate of the radiative efficiency for standard geometrically thin, optically thick accretion disks. This is approximately 16 percent for the  $a/M = 0.9$  black hole spin assumed in our simulations. Clearly the dissipation associated with shocks in accretion flows with even the modest tilts considered here can be a substantial contributor to the overall dissipation of accretion power.

#### 4. DYNAMICS ASSOCIATED WITH THE SHOCKS

In their analysis of radially extended coherent variability in tilted accretion flows, Henisey, Blaes & Fragile (2012) showed that the two high density arms in the inner parts of the accretion flow are located immediately downstream of the two standing shocks, and that structures associated with the variability (transient density clumps and associated spiral acoustic waves) orbit through the density arms. This strongly suggests that the density arms are regions of post-shock compression across which material continues to move. This differs from the interpretation of Fragile et al. (2007), which had these density arms being actual fluid flow streams (“plunging streams”), launched toward the black hole because geodesic orbits are unstable close to the hole and/or the shocks extracted sufficient angular momentum from the flow that streamlines turn toward the hole after crossing the shock surfaces. As illustrated in Figure 3, we likewise find that the shock structures are clearly upstream of the overdense arms, and this is consistent with both previous interpretations.

To understand the true nature of the high density arms, we here investigate the fluid dynamics in their vicinity by examining the actual fluid trajectories. We computed these trajectories using the simulation data dumps of coordinate three-velocity  $V^i \equiv u^i/u^t$  interpolated in both space and time. To advance a trajectory, we computed an interpolated velocity at the current trajectory position and then used this to advance the trajectory a constant time-step. We chose this time step to be smaller than the nominal orbital time  $2\pi(r^{3/2} + aM^{1/2})/M^{1/2}$  at the smallest simulation radii, divided by the number of azimuthal grid zones in the simulation. As noted previously, our simulation data dumps are separated by  $\simeq 3.955M$  in Kerr-Schild coordinate time, corresponding to  $\simeq 1/7$  of an orbital period for the equatorial ISCO orbit at  $r \simeq 2.32M$ . Our trajectories should therefore be reasonably accurate even near the black hole, provided we do not integrate them for much longer than an orbital period, and will be increasingly accurate further away from the hole.

We selected grid points inside one of the density arms, and then integrated the trajectories both forward and backward in time. For simplicity, we first restricted the starting grid points to all lie on one radial shell ( $r = 2.03M$ ). Then, in order to get points inside one arm, we chose points in the upper hemisphere where the density exceeded the density of the contour chosen to illustrate the arms shown in Figure 3. For clarity of visualization,

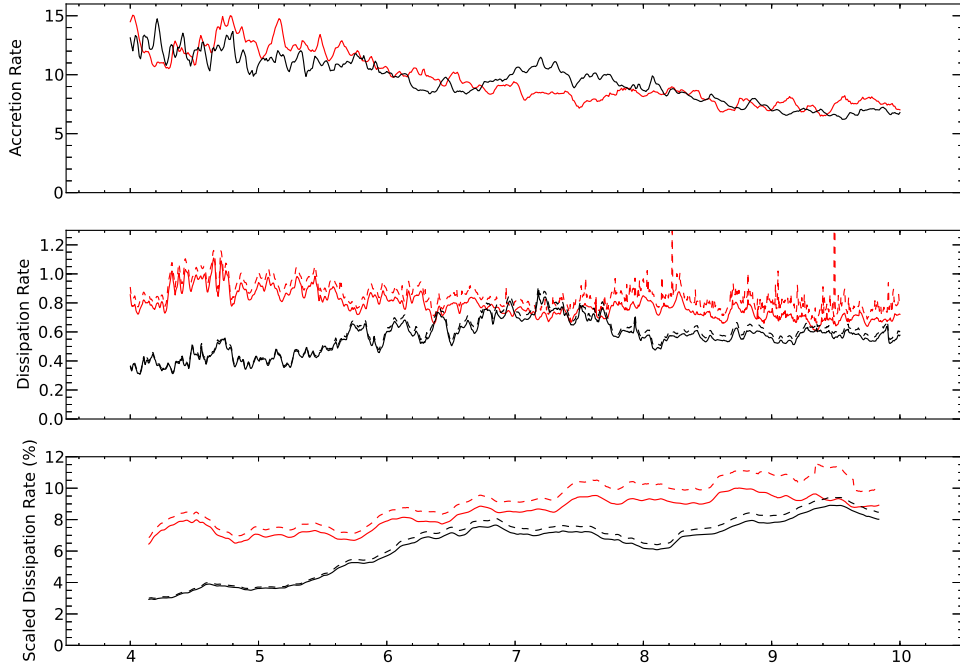


**Figure 1.** Instantaneous accretion rate into the hole (top, in arbitrary units), volume-integrated dissipation rate due to artificial viscosity (middle, in arbitrary units), and volume-integrated dissipation rate scaled by the instantaneous accretion energy  $\dot{M}c^2$  into the hole smoothed over a local time interval of  $237M \simeq 0.3 t_{\text{orb}}$  (bottom). Black curves refer to the  $10^\circ$  simulation, while red curves refer to the  $15^\circ$  simulation. Dashed curves represent the full volume-integrated dissipation rate in each simulation, while solid curves exclude the dissipation inside the coordinate radius of the equatorial direct photon orbit as a crude estimate of how much of the dissipation, if emitted locally, might reach an observer at infinity.

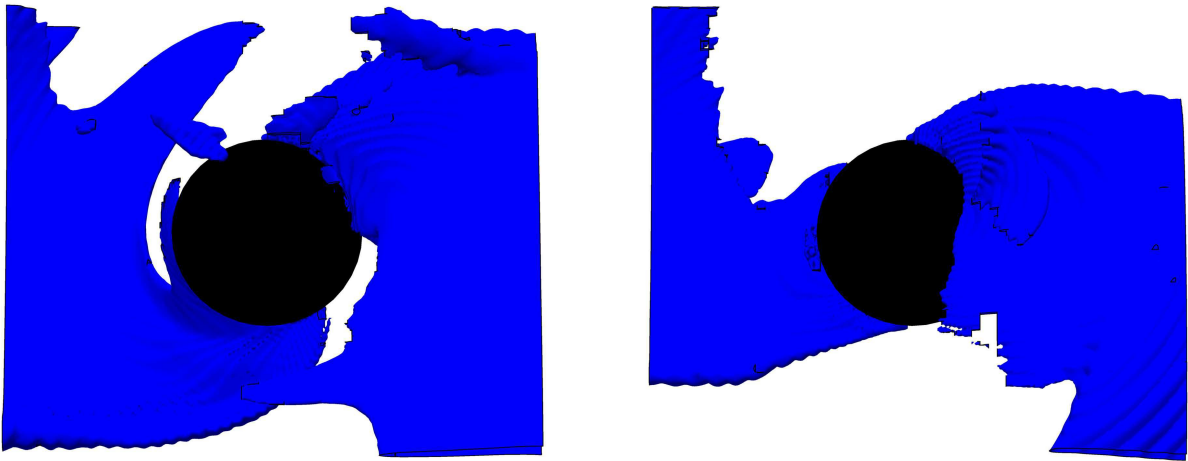


**Figure 2.** Close-up (within a box  $8M$  on a side) of the surface enclosing ninety percent of the dissipation at epoch  $9.95 t_{\text{orb}}$  for the  $10^\circ$  simulation (left) and the  $15^\circ$  simulation (right). The viewing orientation is directly down the spin axis of the black hole, and the flow in both simulations is orbiting counterclockwise in this view. The line of nodes between the black hole equatorial plane and the plane of the initial torus is horizontal in the viewing angle of these figures. As is particularly evident in the  $15^\circ$  simulation on the right, two shock surfaces have formed, one to the left and below the black hole equatorial plane (i.e. behind the black hole in this viewing angle), and one to the right and above the black hole equatorial plane (i.e. in front of the black hole in this viewing angle).

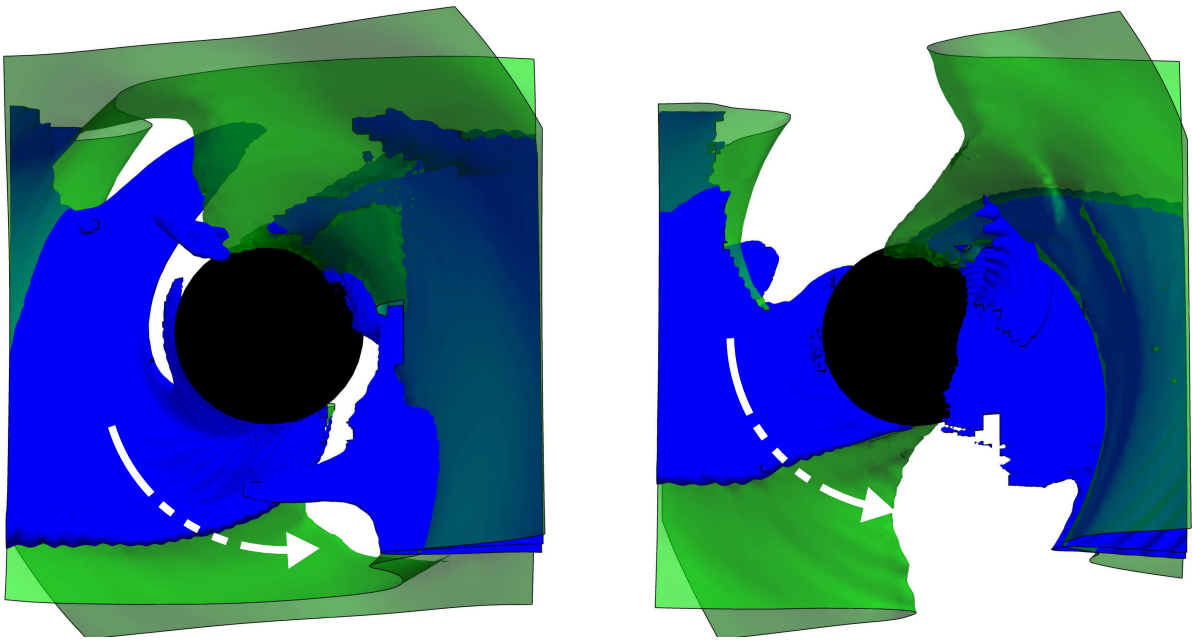


**Figure 3.** Surface enclosing ninety percent of the dissipation (blue, identical to that shown in Figure 2) and a constant density surface (green) for the  $10^\circ$  simulation (left) and the  $15^\circ$  simulation (right), both at epoch  $9.95 t_{\text{orb}}$ , within a box  $8M$  on each side. The viewing orientation is exactly the same as in Figure 2), again looking directly down the spin axis of the black hole, so that the sense of rotation of both the hole and the flow is counterclockwise. The arrows show the sense of a typical shock-crossing trajectory before (solid) it hits the left shock surface (blue), then is behind the shock surface (dashed) in the compressed density region (green), and then emerges from the compressed density region (solid). The overdense regions (green) clearly lie immediately downstream of the shock dissipation surfaces (blue).

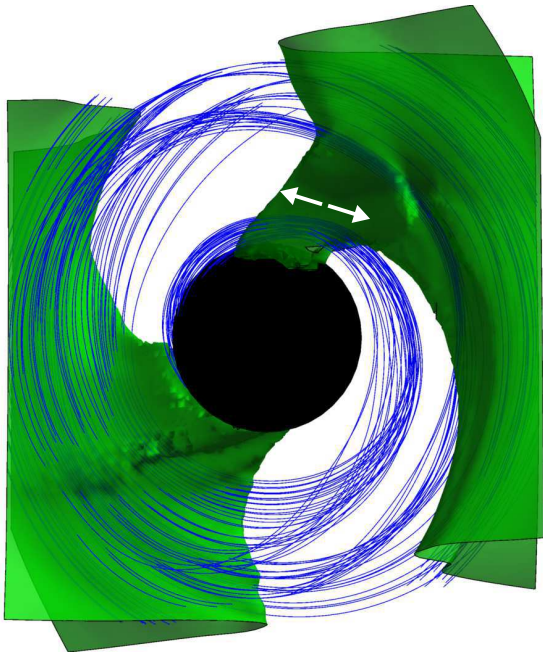


**Figure 4.** The same constant density surface (green) as shown in the right hand panel of Figure 3, with the same viewing orientation, together with selected fluid element trajectories (blue curves) for the  $15^\circ$  simulation at epoch  $9.95 t_{\text{orb}}$ . These trajectories were calculated by starting forward and backward integrations at points within one of the shock dissipation surfaces, as illustrated by the double arrow in the figure. Fluid flows along these trajectories in a counterclockwise sense.

we then used only every fourth trajectory.

Figure 4 shows the resulting trajectories for the  $15^\circ$  simulation near epoch  $9.95 t_{\text{orb}}$ , that were integrated both forward and backward in time starting from inside the density arm in the upper right of the figure. All the fluid trajectories clearly pass *through* the high density arm, which therefore must represent a post-shock compression region rather than a flow stream. The trajectories themselves still represent plunging orbits, in that they spiral into the hole without going around many times, and this is consistent with the fact that spheroidal test particle orbits (non-equatorial geodesics with constant coordinate radius) are unstable in this region (Fragile et al. 2007). Note, however, that these particular fluid trajectories are not themselves geodesic orbits at large radii, as pressure forces keep them moving above (or below) the disk mid-plane.

## 5. STRENGTH OF SHOCKS

As noted in the introduction, Fragile & Blaes (2008) claimed that the strengths of the pairs of shocks formed in these tilted accretion flow simulations were quite modest, but we now show that in fact they are quite strong. One way to do this is to directly measure the upstream Mach number of the shock at a particular point along its surface, but this is nontrivial because of the complicated geometry of both the shock and the tilted accretion flow. We have instead adopted the strategy of computing actual fluid trajectories in the vicinity of the shock surfaces, interpolating fluid rest frame pressure and rest mass density in space and time onto those trajectories, and then measuring the jumps in these quantities that are caused by the shock. The ideal hydrodynamic relativistic shock jump conditions then imply that the upstream spatial

three velocity component normal to the local plane of the shock in the shock rest frame is given by (e.g. Anile 1989):

$$v_+ = \left[ \frac{P_- - P_+}{\rho_+^2 (\tau_+ - \tau_-) + P_- - P_+} \right]^{1/2}, \quad (6)$$

where the subscripts + and - refer to upstream and downstream, respectively. The quantity  $\tau$  is the dynamical volume,

$$\tau \equiv \frac{P + \rho + e}{\rho^2}. \quad (7)$$

The upstream Mach number is then just  $\mathcal{M}_+ \equiv v_+/c_{s+}$ .

These formulas assume that magnetic pressure and tension are completely negligible in the shock dynamics. We enforced this by only using trajectories along which the local fluid rest frame magnetic pressure was less than one tenth of the local fluid rest frame gas pressure everywhere.

We measured jumps in pressure and density along the fluid trajectories as they cross the shock surfaces. For each point on the shock surfaces shown in Figure 3 we calculated short trajectory segments going forward and backward in time. To ensure our measurements remain local, we restricted both the forward- and reverse-time trajectory segments to ten azimuthal zones (twenty for the combined trajectory). We experimented with the length of trajectory segments calculated and found that increasing the number of azimuthal zones slightly (from ten to fifteen) does not affect our results. In order to precisely measure the pre- and post-shock pressures and densities, we also measured the artificial viscosity dissipation rate per unit volume  $[-Q\partial_i(WV^i)]$  in equation (1) along the trajectories. This generally exhibits a very sharp maximum near the shock surfaces. Thus, we chose to measure pre- and post-shock fluid quantities at positions on either side of the dissipation peak where the dissipation rate dropped to below eleven percent of its maximum. Any trajectory segment for which this did not occur was excluded. We experimented with different percentage thresholds (i.e. five and twenty percent) and found that the maximum upstream Mach numbers, Lorentz factors and compression ratios changed by at most five percent. (Interestingly, measurements for individual trajectories were not as robust. For example, we took trajectories corresponding to the maximum Mach number for a given threshold and measured the changes in the quantities for each individual trajectory in this set. We found that the shock quantities could change by as much as twenty percent. In fact, trajectories corresponding to maximum shock quantities for our nominal threshold could be rejected for other choices of threshold. While these details may merit further investigation, they are not particularly important for the purposes of obtaining a rough estimate of overall shock strength.) As an independent verification of whether these provided good pre- and post-shock measurements, we also checked how well they satisfied the Taub adiabat (e.g. Anile 1989), which may be written

$$\frac{(P_- - P_+)(\tau_- + \tau_+)}{\rho_-^2 \tau_-^2 - \rho_+^2 \tau_+^2} = 1. \quad (8)$$

We only considered trajectories for which the difference

between the left hand side and unity was less than five percent over the shock surfaces. Figure 5 shows an example of fluid quantities measured along one particular trajectory that we considered acceptable at epoch  $9.95 t_{\text{orb}}$  in the  $15^\circ$  tilt simulation.

Figures 6 and 7 show the distribution of upstream Mach numbers, Lorentz factors, and density compression ratios across the shock surfaces at epoch  $9.95 t_{\text{orb}} \simeq 7871M$  in the  $10^\circ$  and  $15^\circ$  tilted simulations, respectively. The shock surfaces in these figures have projected radial extents  $\lesssim 10M$ , consistent with the radial extent of significant entropy generation measured in these simulations (Fragile & Blaes 2008; Henisey, Blaes & Fragile 2012). The shocks are mildly relativistic, with upstream Lorentz factors of at most 2 in the  $10^\circ$  tilt simulation and 1.9 in the  $15^\circ$  tilt simulation at this particular epoch, and even these Lorentz factors are only achieved very close to the black hole ( $r = 1.5M$  and  $1.6M$ , respectively, compared to the horizon radius of  $1.44M$ ). However, the shocks are nevertheless strong, with upstream Mach numbers  $\mathcal{M}_+$  as high as 4.3 at approximately  $r = 2.3M$  and 4.7 at approximately  $3.4M$  for the  $10^\circ$  and  $15^\circ$  tilted simulations, respectively, at this particular epoch. Density compression ratios are also strong, as high as 4.8 and 5 for  $10^\circ$  and  $15^\circ$ , respectively, at this particular epoch. This is somewhat higher than the maximum value of 4 expected for a non-relativistic shock, and these high compression ratios are occurring near the black hole where the Lorentz factors of the flow through the shock are somewhat higher than unity. The highest Mach numbers are actually achieved further out in radius, where the compression ratios are 4.3 and 4.1 for the  $10^\circ$  and  $15^\circ$  simulations, respectively.

Table 1 summarizes the properties of the shocks at positions of maximal upstream Mach number at this epoch as well as three earlier epochs, in both simulations. Also listed are the locations and values where the shocks achieve maximal upstream Lorentz factor and compression ratio. The maximal Mach numbers vary considerably with epoch, ranging from 3 to 4.6 for  $10^\circ$  and 4.7 to 6 for  $15^\circ$ . The maximal upstream Lorentz factors never exceed 2 for all the tilts and epochs considered here. Material is also strongly compressed with the compression ratio exceeding 4 for 2 of the 4 epochs for  $10^\circ$  and all 4 epochs for  $15^\circ$ . The maximum Mach number generally occurs further out in radius from the point of maximal compression. Although the shock properties vary over time, the shocks are consistently strong and only mildly relativistic.

Our previous claim that the shocks were quite weak was based in part on the fact that there exist regions in the flow which are strongly magnetized (low plasma beta), and visually these regions appeared to be associated with the post-shock regions of the flow (Fragile & Blaes 2008). However, our more detailed, quantitative analysis here shows that much of the shock surfaces are actually associated with *weakly* magnetized fluid trajectories. Our previous argument was therefore incorrect, and the shocks are in fact strong. In this paper, we focused on weakly magnetized trajectories, purposely excluding trajectories passing through strongly magnetized regions.

## 6. CONCLUSIONS

In general, there is no reason to expect the angular momentum of the fuel source in a black hole accretion disk to have any causal connection to the spin of the hole itself, unless there has been sufficient time for alignment to take place. This suggests that tilted accretion flows could be quite common in nature, particularly in the case of supermassive black holes which frequently receive new sources of fuel. Two mechanisms have been proposed that can plausibly align a black hole and a tilted accretion disk. A geometrically thin disk could be aligned by the Bardeen-Petterson effect (Bardeen & Petterson 1975; Sorathia, Krolik & Hawley 2013b). More recently, an MHD alignment mechanism associated with magnetically arrested accretion was found to be effective in aligning geometrically thick disks (McKinney, Tchekhovskoy, & Blandford 2013). Nonetheless, there are GRMHD simulations of geometrically thick flows where the disk remains misaligned with the spin of the hole (Fragile et al. 2007).

Such simulations of hot tilted flows exhibit striking qualitative differences in the innermost regions from untilted flows: notably, a pair of standing shocks and a pair of high density arms. Fluid trajectories pass through the high density arms, which are therefore regions of post-shock compression, rather than streams of material plunging into the hole as claimed by Fragile et al. (2007). The shocks themselves are quite strong, though only mildly relativistic, with upstream Mach numbers as high as  $\simeq 4.6 - 6$  for tilt angles of  $10^\circ - 15^\circ$ . Dissipation within the shocks amounts to a substantial fraction (3 – 12 percent) of  $\dot{M}c^2$ . A steady-state has not yet been achieved in the simulations analyzed in this paper, and the dissipated fraction of  $\dot{M}c^2$  actually slowly increases with time. This is because the shocked regions expand outward and dissipate larger fractions of the accretion power.

It is natural to ask how the shocks would affect the observed properties of the accretion flow. Synthetic images, spectra and variability of simulated tilted accretion flows produced by post-processed general relativistic ray tracing calculations have been produced in recent years using a number of emission models (Dexter & Fragile 2011, 2013). In the context of the Galactic Center source Sgr A\*, the emission was assumed to be thermal synchrotron with a spatial and temporal electron temperature distribution that is in fixed proportion to the ion temperature measured from the simulations (Dexter & Fragile 2013). Synthetic images under these assumptions are strongly dominated by the shock structures, particularly when viewed face-on. Moreover, the electron temperatures get high enough that the spectra can reproduce the observed near infrared emission from this source. That the shocks are playing such a dominant role may in part be because of the assumed emission model: the internal energy evolution scheme of the simulations means that the only heating that occurs is near shocks, and so that is where the electron temperatures will be high. However, the fact that we find that the dissipation produced by the shocks is a substantial fraction of  $\dot{M}c^2$  implies that the shocks should be a very important contributor to the emission from tilted accretion flows, regardless of the assumed emission mechanism. For example, Dexter, Agol & Fragile (2009) esti-



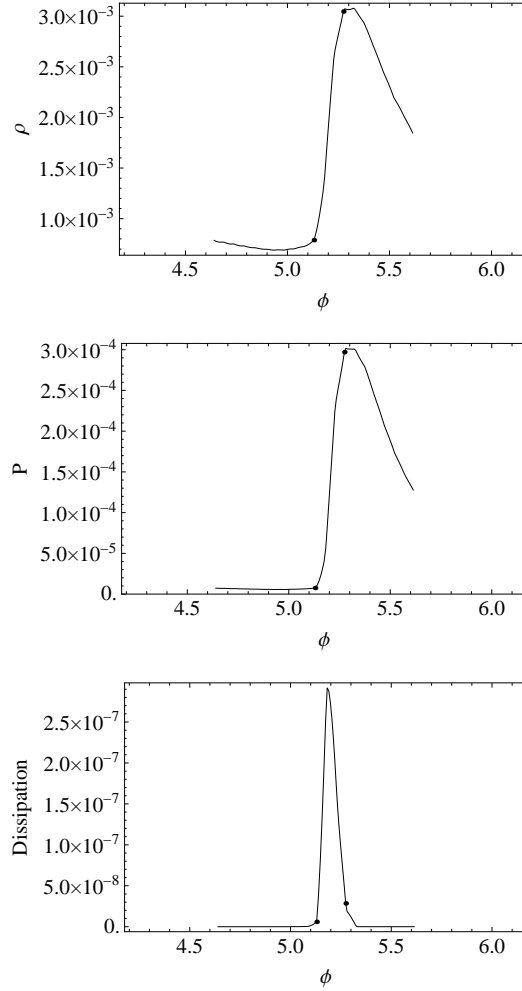


**Figure 5.** Density  $\rho$ , pressure  $P$ , and dissipation rate per unit volume, all in code units, along one particular trajectory as it crosses the shock surface at epoch 9.95  $t_{\text{orb}}$  in the  $15^\circ$  tilt simulation. Dots show the locations where pre- and post-shock quantities were measured.

**Table 1**  
Shock Properties at Various Epochs and Locations

Tilt ( $^\circ$ )	Epoch ( $t_{\text{orb}}$ )	Maximum Upstream ( $r/M, \vartheta, \varphi$ ) <sup>a</sup>	Upstream Mach Number $v_+/c_s$	Mach Number $\gamma(v_+)$	$\rho_-/\rho_+$	Maximum Upstream Lorentz Factor ( $r/M, \vartheta, \varphi$ ) <sup>a</sup>	$\gamma(v_+)$	Maximum Compression Ratio ( $r/M, \vartheta, \varphi$ ) <sup>a</sup>	$\rho_-/\rho_+$
10	4.05	(2.5,2.1,3.1)	3.0	1.1	3.3	(1.6,1.6,1.7)	1.1	(2.3,1.8,3.8)	3.4
10	6.00	(3.6,1.3,6.0)	3.8	1.1	3.6	(1.5,1.8,4.0)	1.5	(1.5,1.8,4.0)	3.9
10	8.00	(4.7,1.7,2.7)	4.6	1.2	3.9	(1.5,0.81,6.0)	1.5	(3.2,1.8,3.1)	4.1
10	9.95	(2.3,0.99,5.1)	4.3	1.5	4.3	(1.5,1.1,5.9)	2.0	(1.5,1.1,5.9)	5.0
15	4.05	(2.8,1.9,2.9)	4.7	1.3	4.1	(1.6,2.3,1.9)	1.4	(2.3,1.9,3.1)	4.4
15	6.00	(2.4,1.2,6.1)	6.0	1.5	4.5	(1.5,0.92,6.1)	1.6	(2.1,1.2,6.2)	4.7
15	8.00	(4.1,2.1,1.9)	5.0	1.2	4.0	(1.5,2.3,2.6)	1.9	(1.7,2.3,2.6)	4.9
15	9.95	(3.5,1.0,5.2)	4.7	1.2	3.9	(1.6,2.2,2.3)	1.9	(1.6,2.2,2.3)	4.8

<sup>a</sup> Locations in tilted Kerr-Schild coordinates

mate that of order ten percent of  $\dot{M}c^2$  is lost by magnetic reconnection in an untilted simulation completed using the same, non-energy conserving code that we use here. Shock dissipation is therefore likely to be comparable to turbulent dissipation in tilted accretion flows.

Particularly in the collisionless conditions of the Sgr A\* flow, the presence of standing shocks could also lead to particle acceleration and nonthermal electron energy distributions. We find that the shocks are strong, but not

very relativistic, with compression ratios of at most 5. Standard first order Fermi acceleration models would therefore predict synchrotron surface brightness spectral indices ( $I_\nu \propto \nu^\alpha$ ) as flat as  $\alpha = -0.4$ .

We thank the referee for comments that significantly improved this paper, and Jason Dexter for very useful conversations and comments. This work was sup-

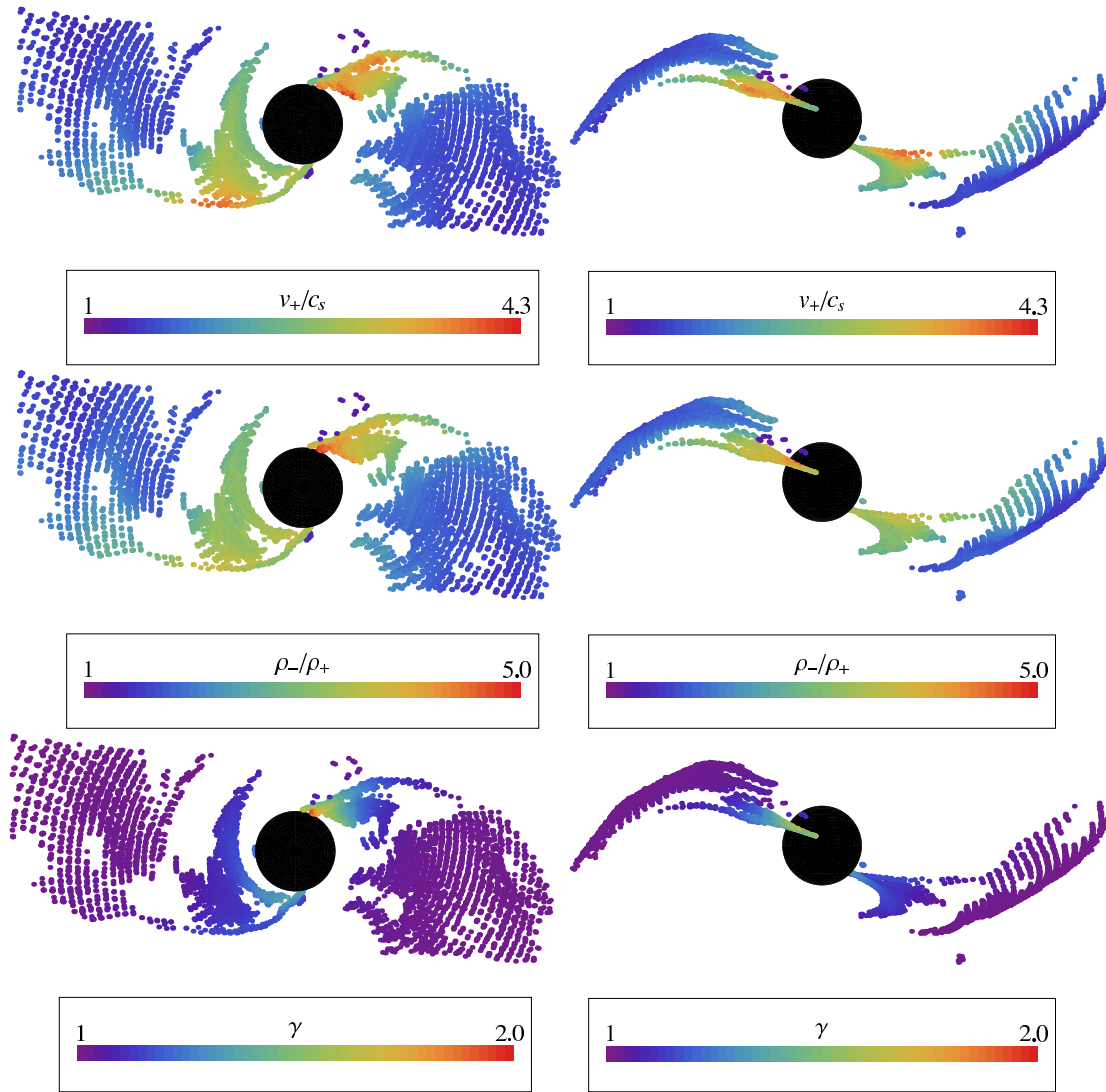


**Figure 6.** Upstream Mach number  $\mathcal{M}_+ = v_+/c_{s+}$  (top row), Lorentz factor  $\gamma(v_+) \equiv (1 - v_+^2)^{-1/2}$  of the upstream three-velocity component  $v_+$  normal to the shock surface in the local shock rest frame (middle row), and compression ratio  $\rho_-/\rho_+$  (bottom row) for the  $10^\circ$  tilt simulation 0910h at epoch  $9.95t_{\text{orb}}$ . The left column figures are viewed from directly above the black hole spin axis, with the line of nodes between the black hole equatorial plane and the plane of the initial torus oriented horizontally (the same viewing geometry as in Figures 2-4). The sense of rotation of both the black hole and the accretion flow is counterclockwise. The right column figures are viewed with the black hole spin axis pointing upward in the plane of the page, and viewed from a direction in the equatorial plane that corresponds to being above the position of the black hole in the left hand column of figures. The line of nodes between the black hole equatorial plane and the plane of the initial torus is still horizontal and in the plane of the page in this view. The figures are to scale (treating the spatial Kerr-Schild coordinates as flat space spherical polar coordinates for constructing these figures), with the filled black circle indicating the location of the event horizon at  $r \simeq 1.44M$ . The horizontal extent of the figures is approximately  $20M$ .

ported in part by National Science Foundation grant AST-0707624. In addition, AG acknowledges support from the Goldwater Foundation and PCF acknowledges support from the National Science Foundation under grants AST-0807385 and PHY11-25915.

#### REFERENCES

- Anile, A. M. 1989, *Relativistic Fluids and Magneto-Fluids* (Cambridge: Cambridge University Press)
- Anninos, P., Fragile, P. C., & Salmonson, J. D. 2005, *ApJ*, 635, 723
- Balbus, S. A., & Hawley, J. F. 1991, *ApJ*, 376, 214
- Balbus, S. A., & Hawley, J. F. 1998, *Rev. Mod. Phys.*, 70, 1
- Bardeen, J. M., & Petterson, J. A. 1975, *ApJ*, 195, L65
- Beckwith, K., Hawley, J. F., & Krolik, J. H. 2006, eprint (astro-ph/0605295)
- Beckwith, K., Hawley, J. F., & Krolik, J. H. 2008, *MNRAS*, 390, 21
- Cuadra, J., Nayakshin, S., Springel, V., & Di Matteo, T. 2006, *MNRAS*, 366, 358
- De Villiers, J.-P., Hawley, J. F., & Krolik, J. H. 2003, *ApJ*, 599, 1238
- Dexter, J., Agol, E., & Fragile, P. C. 2009, *ApJ*, 703, L142
- Dexter, J., & Fragile, P. C. 2011, *ApJ*, 730, 36
- Dexter, J., & Fragile, P. C. 2013, *MNRAS*, 432, 2252
- Font, J. A., Ibáñez, J. M.<sup>A</sup>, & Papadopoulos, P. 1998, *ApJ*, 507, L67
- Fragile, P. C. 2009, *ApJ*, 706, L246
- Fragile, P. C., & Anninos, P. 2005, *ApJ*, 623, 347
- Fragile, P. C., & Anninos, P. 2007, *ApJ*, 665, 1507
- Fragile, P. C., Blaes, O. M., Anninos, P., & Salmonson, J. D. 2007, *ApJ*, 668, 417
- Fragile, P. C., & Blaes, O. M. 2008, *ApJ*, 687, 757
- Gammie, C. F., McKinney, J. C., & Tóth, G. 2003, *ApJ*, 589, 444
- Gillessen, S., Genzel, R., Fritz, T. K., et al. 2012, *Nature*, 481, 51

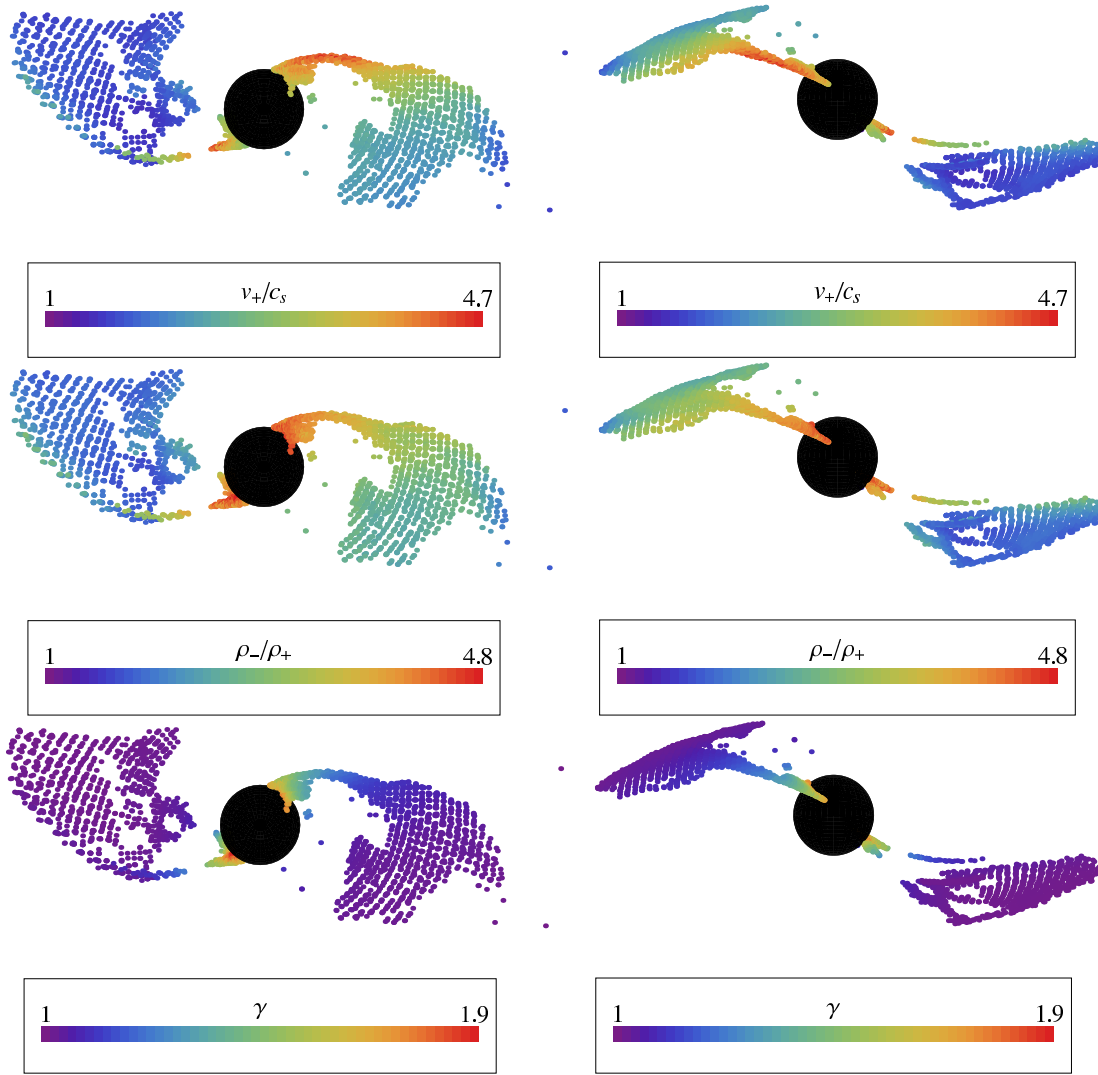


**Figure 7.** Same as Figure 6, only for the  $15^\circ$  tilt simulation 0915h at epoch  $9.95t_{\text{orb}}$ .

Greene, J., Bailyn, C. D., & Orosz, J. A. 2001, *ApJ*, 554, 1290  
 Henisey, K. B., Blaes, O. M., Fragile, P. C., & Ferreira, B. T. 2009, *ApJ*, 706, 705  
 Henisey, K. B., Blaes, O. M., & Fragile, P. C. 2012, *ApJ*, 761, 18, 14 pp.  
 Hjellming, R. M., & Rupen, M. P. 1995, *Nature*, 375, 464  
 Ivanov, P. B., & Illarionov, A. F. 1997, *MNRAS*, 285, 394  
 King, A. R., & Pringle, J. E. 2006, *MNRAS*, 373, L90  
 Krolik, J. H., Hawley, J. F., & Hirose, S. 2005, *ApJ*, 622, 1008  
 Martin, R. G., Tout, C. A., & Pringle, J. E. 2008, *MNRAS*, 387, 188

McKinney, J. C., Tchekhovskoy, A., & Blandford, R. D. 2013, *Science*, 339, 49  
 Noble, S. C., Krolik, J. H., & Hawley, J. F. 2009, *ApJ*, 692, 411  
 Papaloizou, J. C. B., & Lin, D. N. C. 1995, *ApJ*, 438, 841  
 Penna, R. F., McKinney, J. C., Narayan, R., Tchekhovskoy, A., Shafee, R., & McClintock, J. E. 2010, *MNRAS*, 408, 752  
 Sorathia, K. A., Krolik, J. H., & Hawley, J. F. 2013a, *ApJ*, 768, 133, 14 pp.  
 Sorathia, K. A., Krolik, J. H., & Hawley, J. F. 2013b, *ApJ*, in press  
 Steiner, J. F., McClintock, J. E. 2012, *ApJ*, 745, 136  
 Volonteri, M., Sikora, M., & Lasota, J.-P. 2007, *ApJ*, 667, 704